CrossMark

ORIGINAL ARTICLE

A two-dimensional inviscid model of the gravity-current head by Lagrangian block simulation

Vincent H. Chu[1] · Wihel Altai[1]

Abstract A two-dimensional inviscid model of the gravity-current head produced by the release of a relatively small volume of dense fluid from behind a tall lock gate is constructed by Lagrangian block simulation. Three numerical experiments are conducted for the lock's height-to-length aspect ratios $H/L_o = 8$, 4 and 2. The front speeds obtained by the simulations agree with the laboratory observation for a similar range of aspect ratios. The floor velocity in the wake behind these heads is found to be greater than their front speed. The high floor velocity is caused by the impingement of the coherent wake vortex on the floor. It is a condition that permits these gravity-current heads to maintain their structural integrity so that the fine sediments can travel with the head over long distances on the ocean floor. The structural coherence of the current head depends on the lock aspect ratio. The gravity-current head produced by the release from the lock with the highest aspect ratio of $H/L_o = 8$ is most coherent and relatively has the greatest floor velocity and the least trailing current behind the head.

1 Introduction

Gravity current shapes to form a head as the front of the current advances through a surrounding fluid of different density [1, 9, 10, 13, 18]. Sudden release of dense fluids, such as earthquake-triggered turbidities, can produce gravity currents with great destructive forces [8, 21]. As much as 20 m/s of current velocity on the continental slope has been

✉ Vincent H. Chu
   vincent.chu@mcgill.ca

[1] Department of Civil Engineering and Applied Mechanics, McGill University, Montreal,
   QC H3A 2K6, Canada

reported as a consequence of submarine landslides [11]. The total buoyancy in the gravity-current head may increase if the velocity on the floor is sufficiently high to cause re-suspension of the particulate matter from the floor. The advancement of the particulates toward the front and their re-entrainment into the wake is a mechanism responsible for the transport of fine sediments over long distances on the ocean floor [24]. The thickness of the boundary layer can play a critical role in the advance of the gravity-current head. Britter and Simpson [2] have shown how the structure of the head can change depending on slip versus no-slip boundary conditions. At a high Reynolds number, the boundary-layer thickness can be quite small compared with the overall dimensions of the current head. The dynamics of the gravity current over wide ranges of parameter space has been studied in the laboratory by Rottman and Simpson [22], Thomas et al. [25], Marino et al. [15] and Nogueira et al. [18]. The experimental results were correlated mostly in terms of depth-averaged internal hydraulic models. The Direct Numerical Simulations (DNS) model and the Large Eddy Simulations (LES) model have been used by Hartel et al. [9, 10], Thomas et al. [25], Cantero et al. [3, 7] and Ooi et al. [19, 20] to study some aspect of the gravity current in detail. Well-resolved DNS can provide all turbulence-length scales down to the dissipative range. LES with correct modelling of the sub-grid scales can be an efficient alternative, covering a wider range of parameter space utilizing affordable computation resources. DNS were conducted by Cantero et al. [3, 7] up to a Reynolds number of 8950. High Reynolds number LES simulations were carried out by Ooi et al. [20] up to a Reynolds number of 12,600.

The present study is focused on the gravity-current head produced by the release of a relatively small volume of dense fluid behind a tall lock gate. The numerical simulation is based on a two-dimensional inviscid model. The challenge in the numerical simulation is to capture the turbulent interface in the head without the artifact of numerical diffusion. In the classical finite volume method, fluxes are estimated on the surface of the finite volume using a truncation series. Spurious numerical oscillations and false numerical diffusion are the consequences, particularly in regions across sharp discontinuities. Artificial diffusion often is introduced synthetically to gain computational stability. Occasional switching to a diffusive upwind scheme, for example, is one classic strategy to manage the numerical oscillations (see a review of the classical method by Karimpour Ghannadi and Chu [12]). The method of the Lagrangian block simulation (LBS) on the other hand is very different. Fluxes are not estimated so there are no numerical oscillation and diffusion errors from the truncation. Validation of the LBS method has been conducted in the calculation for the advance of wet water on dry bed by Tan and Chu [26, 27] and in the simulations for the laminar-and-turbulent interfaces by Chu and Altai [4–6]. In the absence of spurious oscillations and false diffusion, the best possible inviscid model of the gravity-current head is constructed by the LBS.

2 Lagrangian block simulation

The inviscid model is constructed by setting the real viscosity to zero in the LBS. The general method as delineated in Fig. 1 has a Lagrangian advection step and a diffusion step. The diffusion step however is ignored in the present simulation for the inviscid model. The block-simulation procedure consists of (1) Lagrangian advection, (2) division into portions, and (3) reassembly of the portions into new blocks by the second-moment method. The blocks are renewed in each time increment to prevent excessive distortion.

The numerical error associated with the LBS is not cumulative, and false-diffusion error has been shown to be negligible by Chu and Altai [6]. A couple of simple advection experiments are given in the "Appendix" just to show how the LBS can capture discontinuities without the false diffusion and spurious oscillation errors.

3 Formulation

The LBS for the gravity-current head is based on the Boussinesq approximation, and the two-dimensional stream-function and vorticity formulation. The stream function ψ is introduced to define the x- and y-component of the velocity vector (u, v):

$$u = +\frac{\partial \psi}{\partial y}, \quad v = -\frac{\partial \psi}{\partial x} \tag{1}$$

The vorticity ζ is

$$\zeta = \frac{\partial v}{\partial x} - \frac{\partial u}{\partial y} \tag{2}$$

This definition for the vorticity expressed in terms of stream function ψ is the Poisson equation:

$$\zeta = -\left[\frac{\partial^2 \psi}{\partial x^2} + \frac{\partial^2 \psi}{\partial y^2}\right] \tag{3}$$

The production of the vorticity is determined by the x- and y-momentum equations as follows:

$$\frac{Du}{Dt} = -\frac{1}{\rho}\frac{\partial p}{\partial x} \tag{4}$$
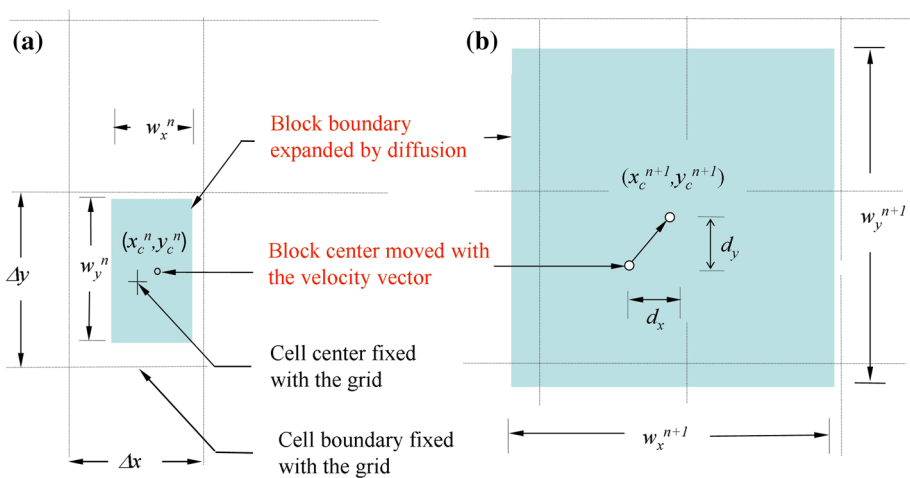

Fig. 1 Lagrangian block in the Eulerian cells **a** before and **b** after the advection and diffusion steps. The Lagrangian block simulation method and the notation details in this figure are given in Chu and Altai [6]

$$\frac{Dv}{Dt} = -\frac{1}{\rho}\frac{\partial p}{\partial y} + g' \tag{5}$$

Subtracting the x-differentiation of Eq. 5 from the y-differentiation of Eq. 4 gives the Lagrangian vorticity equation

$$\frac{D\zeta}{Dt} = \frac{\partial g'}{\partial x} \tag{6}$$

The buoyancy force per unit mass of the fluid is $g' = g(\Delta\rho/\rho)$. The scalar transports of the buoyancy and the vorticity are carried out by Lagrangian block advection without the diffusion step. Two systems of blocks are employed in the simulation. One system of blocks is for the advection of the buoyancy g'. A separate system of blocks is for the advection of the vorticity ζ. The gradients in the Eqs. 4, 5 and 6 are evaluated directly on the Eulerian grid by central differencing. This evaluation for the gradients in the LBS is to be distinguished from the particle methods. In the Smooth Particle Hydrodynamic (SPH) method for example, the gradients are determined by the weighting of the influence by the nearby particles [16].

The numerical solution of the Poisson equation for the stream function and the velocity is obtained by the Gauss–Seidel iteration method. Convergence is declared when the velocity difference between the subsequent iterations is less than 10^{-5} time of the maximum velocity. The simulations are conducted in a tank of a length L equal to four times its height H_{tank} using 384 blocks over the height of the tank and 1536 blocks along the length of the tank. The time-step sizes are such that the Courant number associated with the maximum velocity is 0.2. The dense fluid is released from a small lock of length L_o equal to one-eighth of the tank's height H_{tank}, i.e., $L_o = 1/8H_{tank}$. Three numerical experiments referred to as the full-height, half-height and quarter-height releases are conducted with the height of the lock $H = H_{tank}$, ½H_{tank} and ¼H_{tank}, i.e., $H = 8\,L_o$, $4\,L_o$ and $2\,L_o$, respectively. Figures 2 and 3 show the buoyancy profiles g'/g'_o of the gravity current as the heads advance toward the end of the tank. The height H and length L_o of the locks are defined by the dashed lines in the figures. These releases from a tall lock gate of small volume have produced prominent heads with a weak trailing current behind the heads. The development depends on the height of the lock. For the full-height release with $H = 8\,L_o$ as shown in Fig. 2, the vorticity in the turbulent mixing layer feeding into the wake is able to organize itself to produce one highly coherent vortex within the gravity-current head. In contrast, the current head produced by the half-height release with $H = 4\,L_o$ is less organized as shown in Fig. 3. The structural difference between the coherent structure of the current head in Fig. 2 and the less coherent structure in Fig. 3 will be quantitatively analyzed and explained in the subsequent sections.

4 Front speed at the leading edge

The speed of the front at the leading edge of the gravity-current head is analyzed first. Figure 4 shows front speed u_f normalized by $\sqrt{g'_o H}$ obtained by the LBS for the full-height release, half-height release and quarter-height release. The front speed and the return velocity external to the current head depend on the dam's height H and the tank's height H_{tank}. On average, the front speed tends to decrease slightly due to the entrainment of ambient fluid which moves in the opposite direction to the gravity current. The decrease in
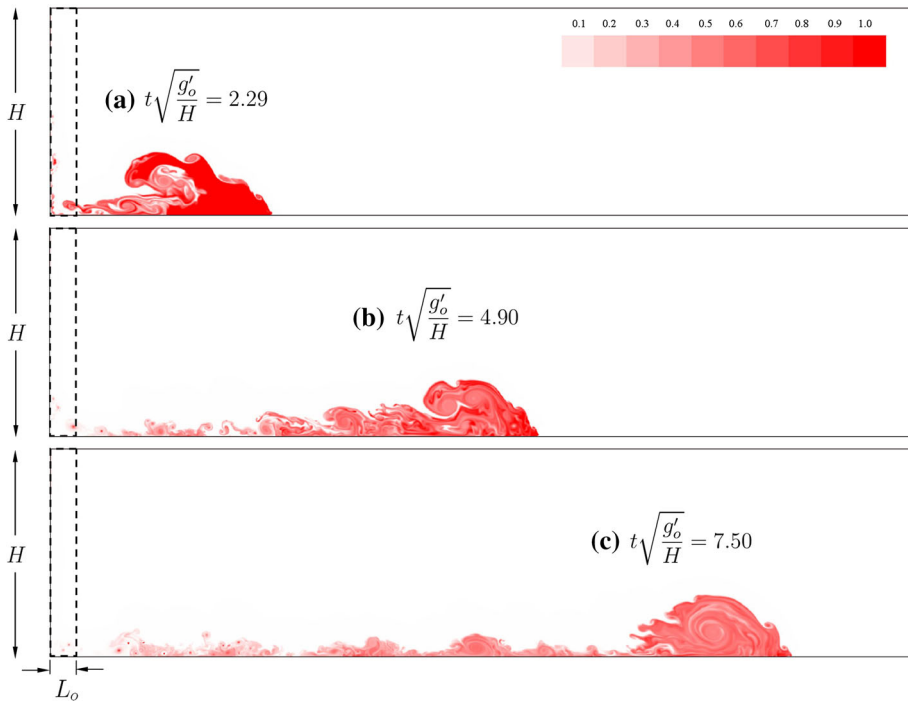
Fig. 2 Development of the buoyancy profiles g'/g'_o of the gravity-current head produced by the full-height release of a source fluid of length L_o and height $H = 8\,L_o$. The *dashed line* marks the initial position of the source fluid of reduced gravity g'_o behind the dam

the front speed is not monotonic. The variations from the monotonic are closely related to the dynamics of the Kelvin–Helmholtz instability in the mixing layer and the feeding of the vorticity from the mixing layer into the wake. This structural dynamics of the current head have been observed and explained in the laboratory experimental study by Nogueira et al. [18].

As pointed out in the laboratory experiment by Rottman and Simpson [22], Marino et al. [15] and Nogueira et al. [17, 18], the development of the gravity current consists of an initial phase when the development is dependent on the initial conditions, and an asymptotic state when the advance of the head is dependent on the total buoyancy at the source. The front speed is zero immediately after the removal of the dam. It accelerates rapidly to a maximum during the acceleration phase. The red open circles in Fig. 4 are the front speeds at the end of the acceleration phase that are obtained by tracing back to the initial positions at $x_f = L_o$. Shin et al. [23] and Marino et al. [15] have examined the role of the ambient current on the front speed. Shin et al. [23] developed a hydraulic theory to correlate the front-speed Froude number to the dam-to-tank height ratio H/H_{tank} by the formula:

$$\frac{u_f}{\sqrt{g'_o H}} = \frac{1}{2}\sqrt{2 - \frac{H}{H_{\text{tank}}}} \tag{7}$$

This theory by Shin et al. [23] and the experimental data of Marino et al. [15] are included in Fig. 5 to compare with the front speeds at the end of the acceleration phase obtained
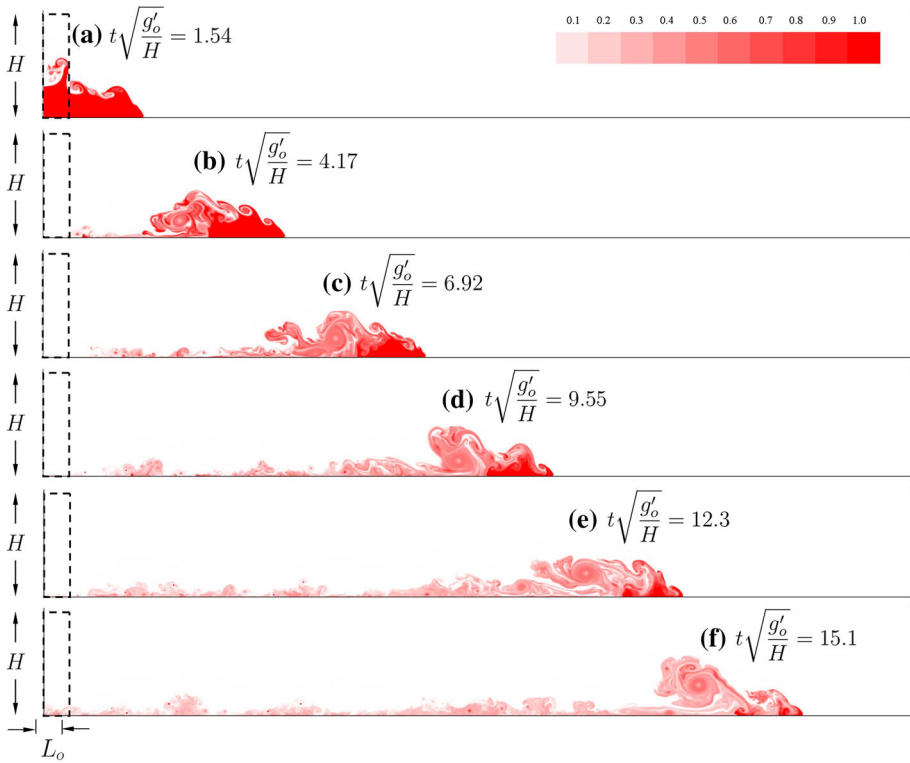
Fig. 3 Development of the buoyancy profiles g'/g_o of the gravity-current head produced by the half-height release of source fluid of a length L_o and a height $H = 4 L_o$. The *dashed line* marks the initial position of the source fluid of reduced gravity g'_o
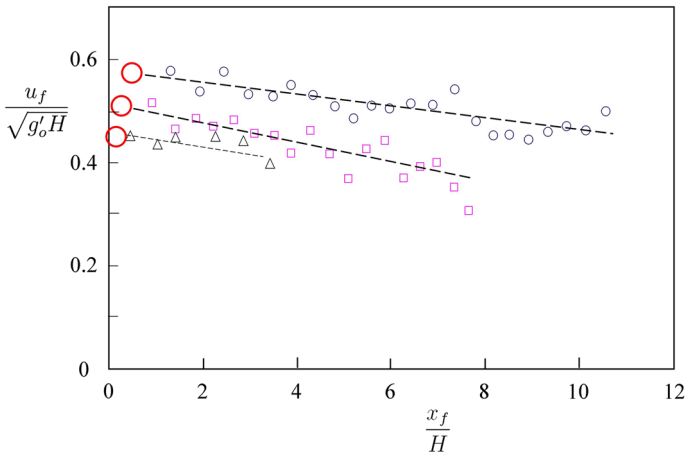

Fig. 4 Front speed u_f plotted versus the front distance x_f from the upstream end of the tank. The *triangular*, *square* and *circle* symbols are the data obtained from full-height, half-height and quarter-height simulations, respectively. The *red open circles* denote the frontal speed at the end of the acceleration phase, which is estimated by tracing back to the initial position of the front at $x_f = L_o$

from the inviscid model simulations. The hydraulic theory of Shin et al. [23] does not include the entrainment. It is therefore not surprising that applying their theory gives a slightly higher front speed than occurs in the results of the experimental data of Marino et al. [15] and the results of the present simulations. However, the agreement between the present inviscid model and the experimental observation of Marino et al. [15] was not entirely anticipated. We offer the following explanation. The data of Marino et al. in Fig. 5 was collected shortly after the acceleration phase in currents of very high Reynolds numbers. In this early stage of development, the inertia effect is still the dominant effect over the viscosity. The inviscid model therefore is an acceptable approximation.

5 Structural coherence of the head by full-height release ($H/L_o = 8$)

The full-height release with the aspect ratio of $H/L_o = 8$ has produced the most coherent structure of the gravity-current head. Figure 2a shows the detachment of this gravity current from the tank at the dimensionless time $t\sqrt{g'_o/H} = 2.29$. The head shown in Fig. 2b for $t\sqrt{g'_o/H} = 4.90$ has multiple eddies in the wake. Finally at time $t\sqrt{g'_o/H} = 7.50$ as shown in Fig. 2c, the wake and the head are combined to form one large coherent vortex. Figure 6 is a close-up view of the vorticity distribution and the velocity of this gravity-current head at the instant after the front has advanced a distance $x_f = 14.9L_o$. The Kelvin–Helmholtz instability initiates the turbulent mixing layer from the leading edge. Vorticity is produced in the mixing layer and then transported along the mixing layer to the back of the gravity-current head to form a wake. A prominent circulation region is observed in the wake region. The maximum velocity occurs at the impingement of the wake vortex on the floor. This full-height release has produced a gravity-current head without much of the trailing current that otherwise would be feeding from behind the head. This is remarkable as the head is now charging forward without much of the current that initiates it. The relation between the head and the gravity current in this full-height release is akin to the formation of a smoke ring and the perfect impulse that blows the ring.
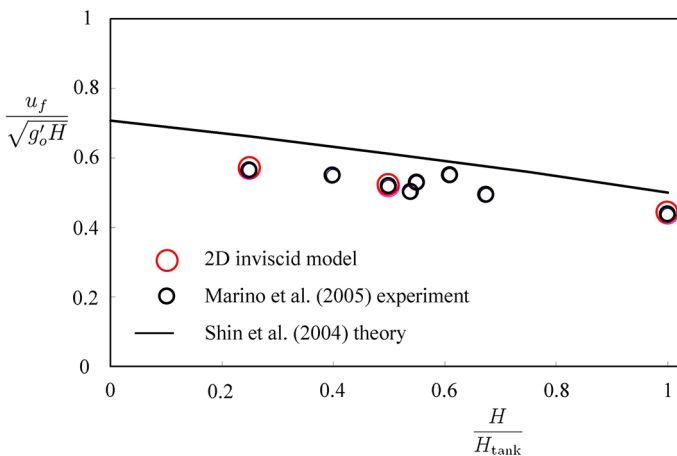

Fig. 5 Frontal speed of the 2D inviscid model compared with the laboratory experimental data by Marino et al. [15] and the hydraulic theory of Shin et al. [23]. The *red open circles* denote the front speed at the end of the acceleration phase obtained from tracing back the LBS data in Fig. 4
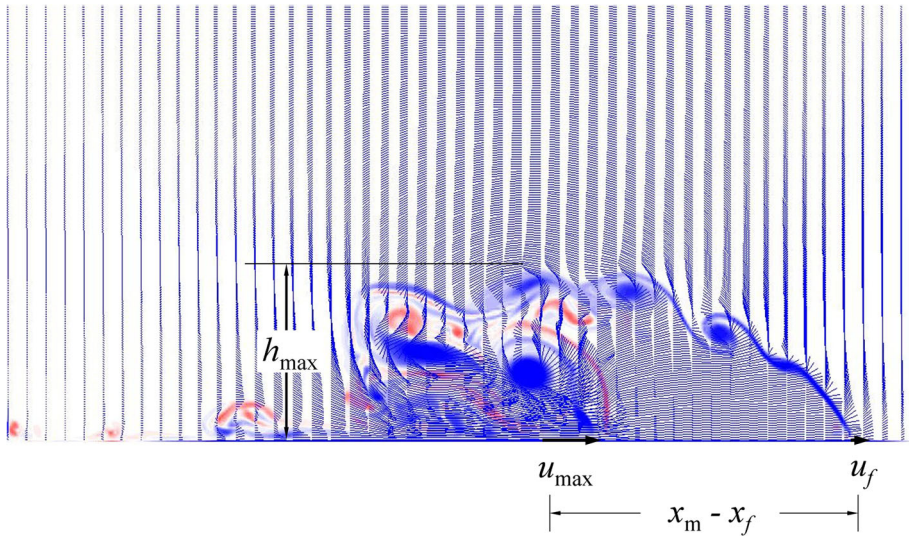
Fig. 6 The vorticity pattern and the velocity vectors delineating the coherent structure of the gravity-current head produced by the full-height release, after the leading edge has advanced a distance $x_f = 14.9$ L_o. The shape of the current head is defined by the current's height h_{max} and the distance $(x_m - x_f)$ from the leading edge to the location where the maximum floor velocity u_{max} occurs

The organization of the vorticity in the wake and the impingement of the coherent wake vortex on the floor have produced a maximum velocity u_{max} in the wake on the floor. The distance from the leading edge to the floor velocity maximum is $(x_f - x_m)$. This length $(x_f - x_m)$ and the maximum height h_m define the shape of the current head. The numerical simulations have determined the maximum floor velocity u_{max}, the length of the head $(x_f - x_m)$ and the height of the head h_m. Figure 7 shows the values of these key parameters: (a) u_{max}/u_f, (b) $(x_f - x_m)/h_{max}$ (c) h_{max}/H, and (d) KE/PE_o, PE/PE_o and $(KE + PE)/PE_o$. The nominal value of the floor maximum velocity is $u_{max}/u_f \sim 3.1$ as the current head advances toward the end of the tank. This is marked as a red dashed line Fig. 7a. There is however considerable variation from this nominal value as the shape of the current head is not entirely constant. The head length-to-height ratio that defines the shape of the gravity-current head has a nominal value of $(x_f - x_m)/h_{max} \sim 1.3$. This and the variation from the value are shown in Fig. 7b. The head-height to the lock-height ratio has a nominal value of $h_{max}/H \sim 0.28$ as shown in Fig. 7c. The height of the gravity-current head h_{max} is determined from the present simulation by the cut off at the 5% boundary where $g'/g'_o = 0.05$.

In the inviscid model the energy is conserved. The potential energy PE and the kinetic energy KE of the gravity-current head are determined from the numerical simulation using the following formulae:

$$PE = \sum_{i=1,M} \sum_{j=1,N} g'_{ij} y_{ij} \quad \text{and} \quad KE = \sum_{i=1,M} \sum_{j=1,N} \frac{1}{2} \left(u_{ij}^2 + v_{ij}^2 \right) \tag{8}$$

in which g'_{ij} is the buoyancy, (u_{ij}, v_{ij}) the velocity components and y_{ij} the elevation at the i–j cell. The grid for the numerical simulations is $i = 1$ to M and $j = 1$ to N in which $M = 1536$ and $N = 384$. Figure 7d shows the variation of the kinetic and potential energy
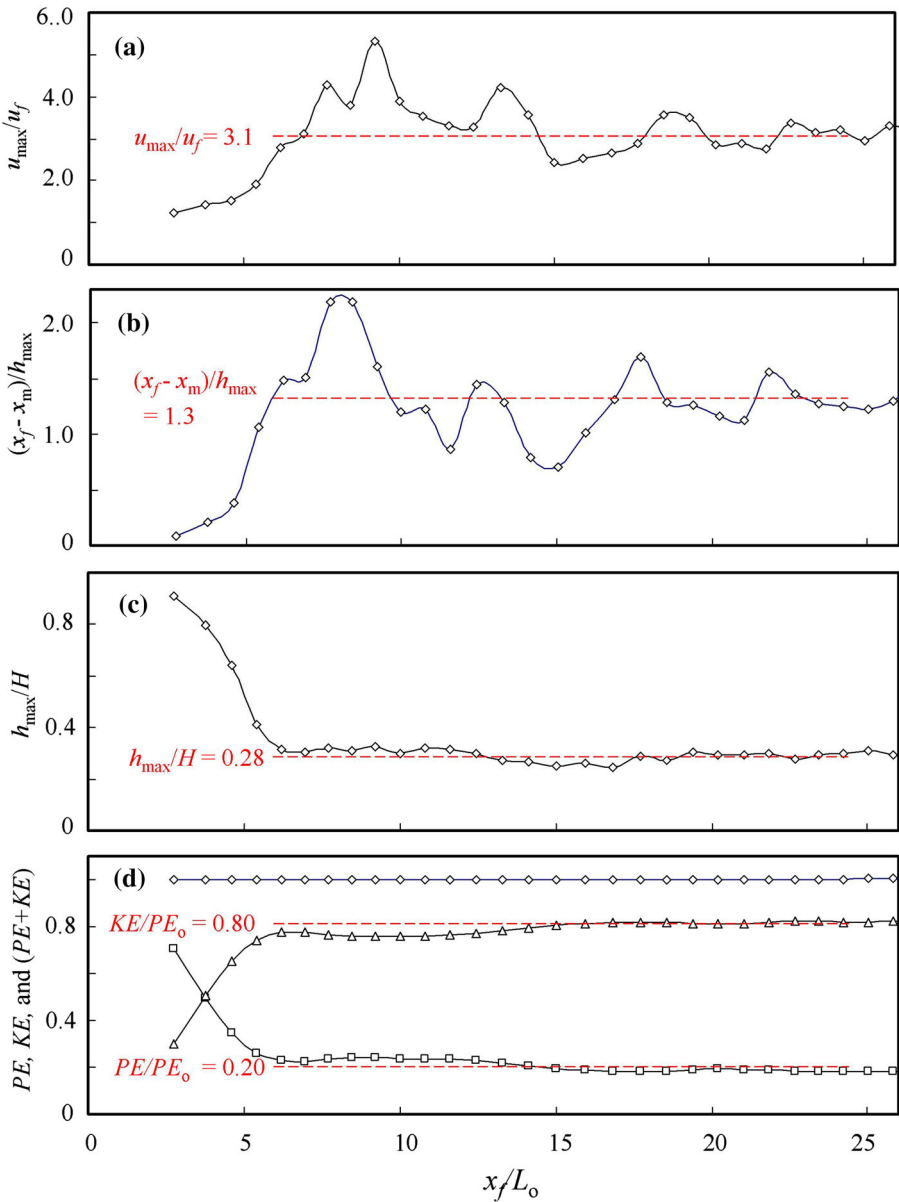
Fig. 7 The key parameters of the gravity-current head produced by the full-height release: **a** u_{max}/u_f, **b** $(x_f - x_m)/h_{max}$, **c** h_{max}/H, and **d** KE/PE_o denoted by the *triangle symbol*, PE/PE_o by the *square symbols* and $(KE + PE)/PE_o$ by the *diamond symbol*. The nominal values for these key parameters are estimated and then marked by the *red dashed lines* in the figure despite the considerable variations from the nominal values

with distance of advance for this gravity-current head produced by the full-height release. The advection of 1536×384 blocks on the grid with 1536×384 cells conserves the energy accurately. Normalized by the initial potential energy PE_o, the kinetic energy

approaches the value of $KE/PE_o \approx 0.80$. The potential energy has a value of $KE/PE_o \approx 0.20$ as the head advances toward the end of the tank. There are some variations in the kinetic energy and the potential energy. The total energy $KE + PE$ is perfectly constant throughout. In this simulation using 1536×384 blocks, the energy ratio $(KE + PE)/PE_o$ is closely equal to unity for all time with an error of no more than 0.27%. Since the energy is conserved in the inviscid model, the deviation from the unity becomes a measure of the accuracy of the numerical simulation.

6 Half-height and quarter-height releases ($H/L_o = 4$ and 2)

The less coherent structure of the gravity-current head is produced by the half-height and the quarter-height releases. The lock height-to-length aspect ratios of these releases are $H/L_o = 4$ and $H/L_o = 2$, respectively, and are comparable to the aspect ratio of $H/L_o = 4$ to 1 in the laboratory experiment of Marino et al. [15] and the $H/L_o = 1.33$ in the laboratory experiment of Nogueira et al. [18]. Figure 3 shows the buoyancy profiles g'/g'_o produced by the half-height release. The gravity-current head now has a wake and a weak current following the wake. The vorticity from the mixing layer organizes itself in the wake into large and small vortexes that interact to produce unsteady dynamic structures with considerable time and space variations. Such unsteady dynamics of the current head in a similar range of lock aspect ratios are well documented and explained by Nogueira et al. [18]. The nominal values of the key parameters of the current head produced by the half-height release and quarter-height release are presented in Figs. 8 and 9 using the same format as in Fig. 7 for the full-height release. There are considerable variations in and deviations from the values of these parameters. Rough estimates of their deviations from the nominal values nevertheless are made. The nominal values are marked by the red dashed lines shown in the figures. Table 1 provides the nominal values and also the rough estimates of the deviations for comparison among the three simulation experiments.

The current head initiated by the full-height release with the highest aspect ratio $H/L_o = 8$ is structurally the most coherent and has the fewest variations among the three simulation experiments. The current head of the full-height release also has the highest relative floor velocity u_{max}/u_f, the smallest length-to-height ratio $(x_f - x_m)/h_{max}$, and the lowest height h_{max}/H compared with the less-coherent current heads produced by the half-height release and the quarter-height release.

7 Energy conservation and computational error

The numerical computation accuracy of the three simulation experiments is not exactly the same. The total energy $(KE + PE)$ would be equal to its initial potential PE_o if the energy were perfectly conserved. The maximum deviation of the ratio $(KE + PE)/PE_o$ from the unity is 0.27% for full-height release, 0.65% for the half-height release and 2.1% for the quarter-height release. These computational errors can be correlated with the number of blocks and cells over the height of the current head. For the full-height release, the height of the current head is $h_{max} \approx 0.28 \, H_{tank}$. The number of computation cells is 108 ($\approx 384 \times 0.28$) over the height of the head. For the half-height and quarter-height releases, the height of the head are $h_{max} \approx 0.42 \, H = 0.21 \, H_{tank}$ and $h_{max} \approx 0.55 \, H = 0.14 \, H_{tank}$. The corresponding numbers are 81 ($\approx 384 \times 0.21$) computation cells and 54 ($\approx 384 \times 0.14$) computation cells over the height of the head. There are fewer
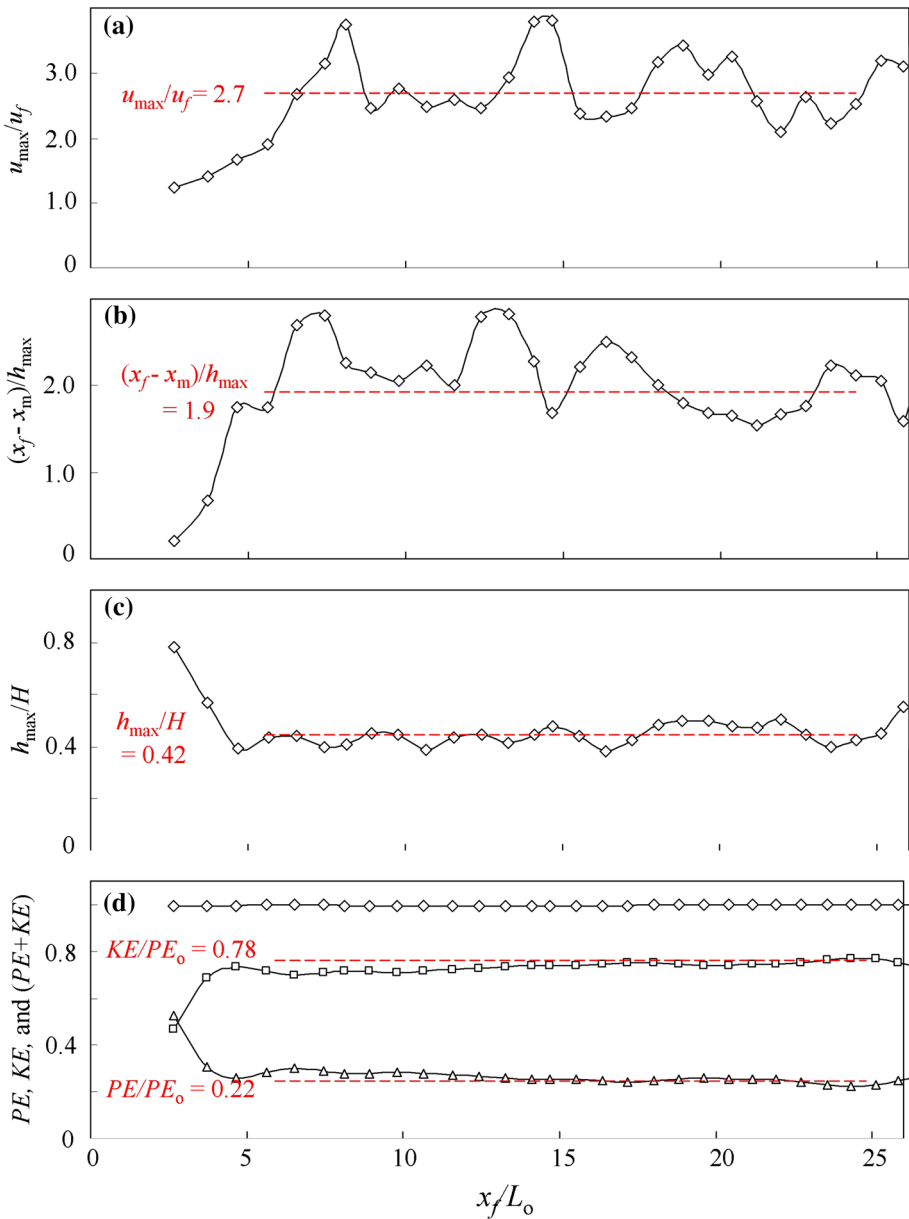
Fig. 8 The key parameters of the gravity-current head produced by the half-height lock release: **a** u_{max}/u_f, **b** $(x_f - x_m)/h_{max}$, **c** h_{max}/H, and **d** KE/PE_o denoted by the *square symbol*, PE/PE_o by the *triangle symbols* and $(KE + PE)/PE_o$ by the *diamond symbol*. For comparison with other simulations, the nominal values for the key parameters are estimated and then marked by the *red dashed lines* in the figure

computation cells over the height of the current head for the half-height and quarter-height releases. This problem of resolution is reflected in the energy conservation. It explains why the ratios $(KE + PE)/PE_o$ for the half-height release and quarter-release deviate from the unity by as much as 0.65 and 2.1%, respectively.
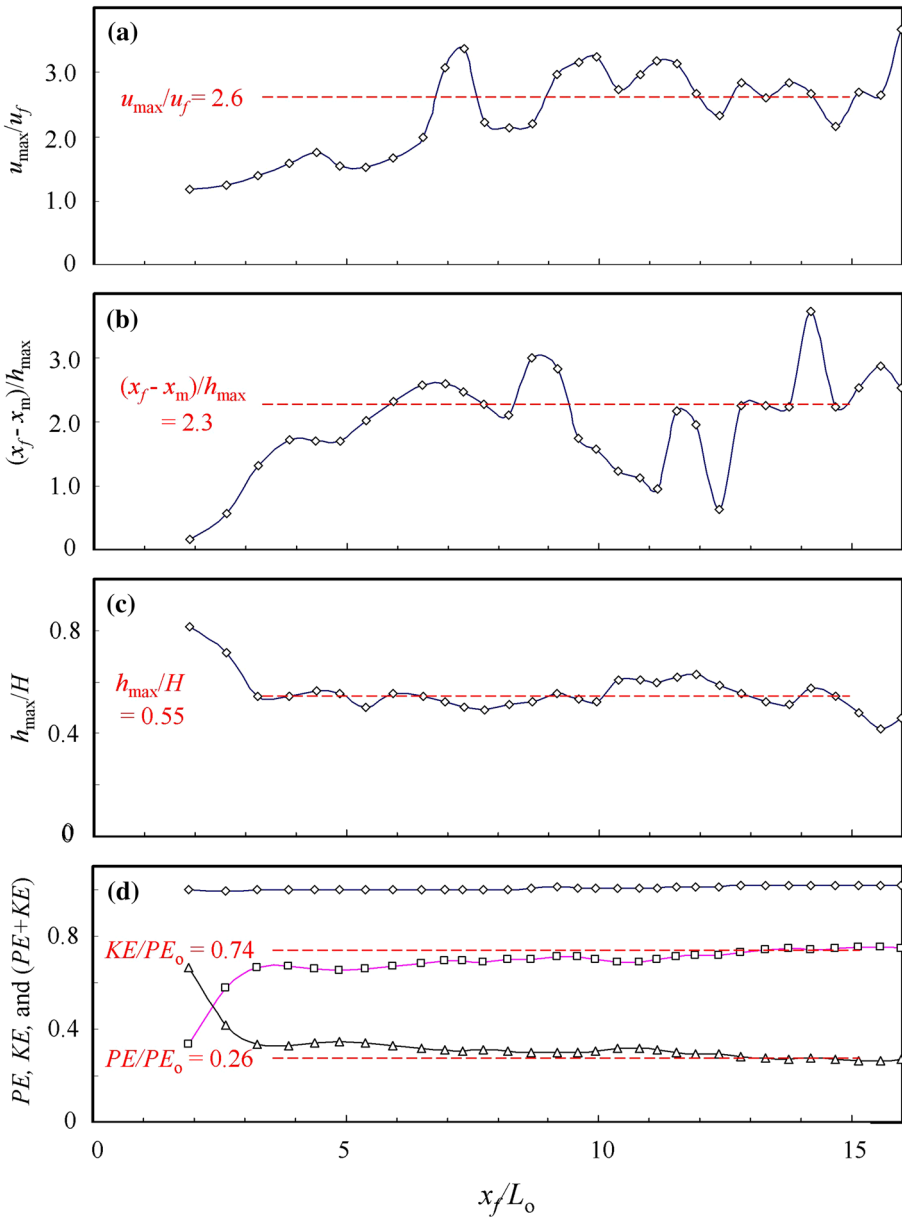
Fig. 9 The key parameters of the gravity-current head produced by the quarter-height lock release: **a** u_{max}/u_f, **b** $(x_f - x_m)/h_{max}$, **c** h_{max}/H, and **d** KE/PE_o denoted by the *square symbol*, PE/PE_o by the *triangle symbols* and $(KE + PE)/PE_o$ by the *diamond symbol*. For comparison with other simulations, the nominal values for the key parameters are estimated and then marked by the *red dashed lines* in the figure

Table 1 Nominal values and deviations from the values of the key parameters for the gravity-current head produced by the full-height, half-height and quarter-height releases

	$u_{\max}/u_f$	$(x_f - x_{\mathrm{m}})/$ $h_{\max}$	$h_{\max}/H$	$KE/$ PE_{o}	$PE/$ PE_{o}	$(KE + PE)/$ PE_o
Full-height ($H/L_{\mathrm{o}} = 8$)	3.1 ± 0.3	1.3 ± 0.4	0.28 ± 0.1	0.8	0.2	1 ± 0.003
Half-height ($H/L_{\mathrm{o}} = 4$)	2.7 ± 0.7	1.9 ± 0.5	0.42 ± 0.8	0.78	0.22	1 ± 0.006
Quarter-height ($H/$ $L_{\mathrm{o}} = 2$)	2.6 ± 0.8	2.3 ± 1.5	0.55 ± 0.8	0.74	0.26	1 ± 0.021

8 Discussion and conclusion

The gravity-current heads produced by the release of a relatively small volume of source fluid from behind a tall lock gate are studied for structural coherence of the current heads. Three LBS based on a two-dimensional inviscid model are conducted for the lock aspect ratios $H/L_o = 8$, 4 and 2. The current head produced by the highest lock aspect ratio $H/L_o = 8$ is most coherent and has the highest floor velocity and the least trailing current behind the head. The simulations based on the two-dimensional inviscid model cannot perfectly reproduce reality. They do however suggest the possibility of a coherent structure with high floor velocity. The association of structural coherence with the floor velocity is significant. The high floor velocity may explain the destructive force of the earthquake-triggered turbidities reported by Heezen and Ewing [8], Piper et al. [21] and Hsu et al. [11]. In a coordinated system moving with the front velocity, the dense fluid is pushed from the back toward the current head with a relative speed equal to $(u_{\max} - u_t)$ and from the front with a relative speed equal to u_t. The convergence of the external flow inward is balanced by the tendency of the dense fluid to spread outward along the floor. This is a necessary condition for a gravity-current head to maintain its structural integrity so that the fine sediments can travel with the head over long distances on the ocean floor without significantly changing the form of the head. The high velocity on the floor could also be responsible for the re-suspension of the fine sediment and possible increase of the total buoyancy within the gravity-current head.

Appendix: Simple advection experiments by LBS and classical method

Since the LBS is not a conventional method, a couple of simple advection experiments are conducted and the results are presented in this appendix to show how LBS can capture sharp discontinuities without diffusion and spurious oscillation errors. The LBS procedure consists of (1) Lagrangian advection, (2) division into portions, and then (3) reassembly of the portions into new blocks by the second-moment method. The blocks are renewed in
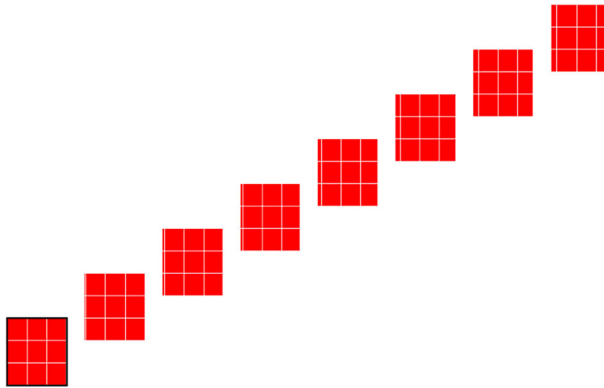
Fig. 10 Simple advection of mass by a uniform velocity oriented at an angle to the grid. The initial position of the 3 × 3 blocks is framed by the *black borderline*. The *white lines* define the Eulerian grid

each time increment to prevent excessive distortion. Figure 10 shows the Lagrangian block advection of mass by a uniform velocity at an oblique angle relative to the cells. The initial position is the 3 × 3 blocks within the black frame in the figure. The simple advection by the LBS gives the exact solution, as the total mass is moved to the new position without changing size and shape. The subsequent images in the figure are the total mass at later times occupied by more than 3 × 3 blocks.

Figure 11a shows the Lagrangian block advection in a non-uniform velocity field produced by the solid-body rotation. The initial profile of the mass is the 4 × 4 blocks within the black frame in the figure. The distortion error in the rotation flow field is the
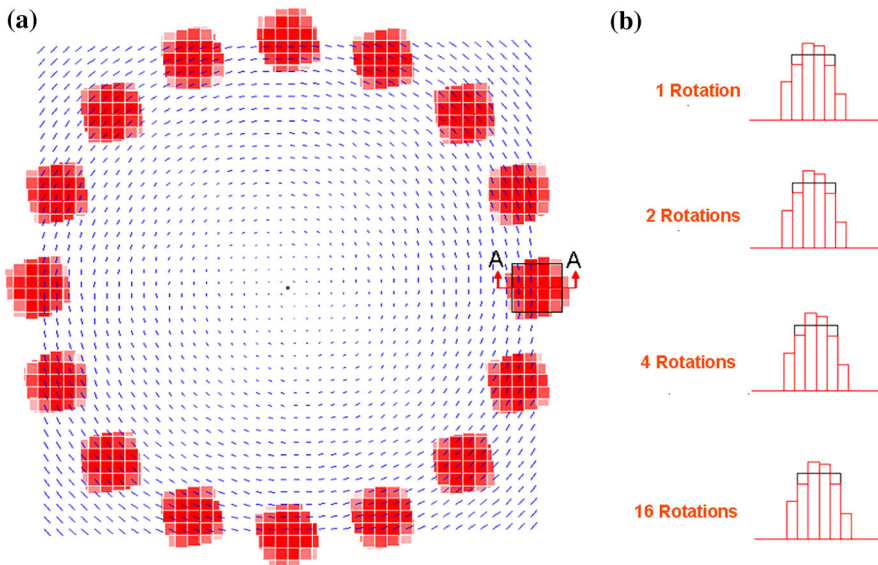

Fig. 11 **a** Sequence of images showing the positions and the mass concentration of the blocks during the advection by a circular velocity field of a solid-body rotation. **b** The concentration profile at the cross-section *A–A* after advection of the mass by the circular velocity field of 1, 2, 4 and 16 rotations. The *black-colored frame* defines the exact solution
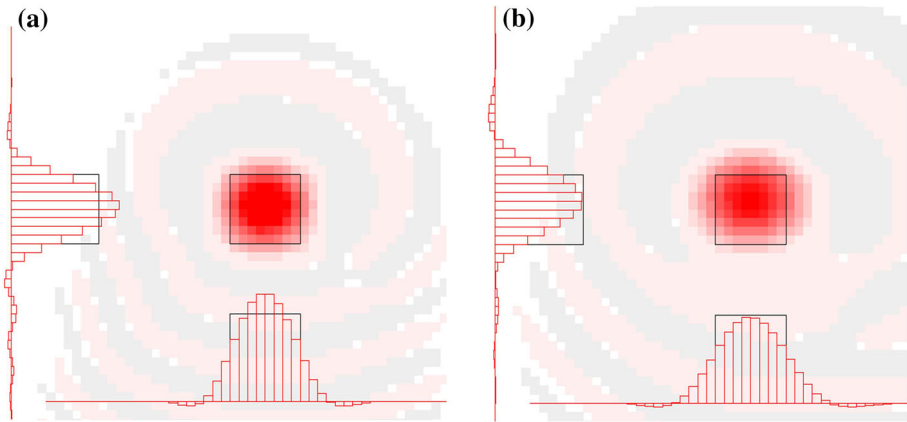
Fig. 12 Mass-concentration profiles after completing **a** 1 solid-body rotation and **b** 4 solid-body rotations. The computations were conducted using the classical finite volume method known as the QUICKEST. The mass concentration profiles in the cross-sections passed through the mass center are shown on the *left-hand side* and the *bottom side* of the figure. The frame in the *color of black* defines the exact solution

over-shooting of the mass concentration above its initial value in the central region, and the spillover of the masses to the side. This distortion error may be significant in simulation using a coarse grid. However, the error is not cumulating. The mass-concentration profiles are the same after 2, 4 and 16 rounds of the rotation, as shown in Fig. 11b.

The computation error with the classical finite element method is very different. For comparison, the simulation for the same rotation flow field was carried out using the classic QUICKEST scheme by Leonard [14]. The results are shown in Fig. 12. Significant false diffusion and spurious oscillation errors are observed after 1 solid-body rotation. Further error is produced after 4 solid-body rotations. Like many classical methods, the simulation error by the QUICKEST is oscillatory. The spurious numerical oscillations would lead to computational instability, which is a severe problem associated with the use of the classical finite volume method (see e.g., Karimpour Ghannadi and Chu [12] for discussion of the classical method). The QUICKEST simulation shown in Fig. 12 actually collapsed shortly after the 4th rotation.

The LBS method conceptually is a significant departure from the Eulerian finite volume method (FVM). The formulation for the LBS also is distinctively different from the particle methods. In the SPH method for example, the gradients are determined by the weighting of the influence by the nearby particles [16]. In contrast, the gradients in the Eqs. 4, 5 and 6 are evaluated directly on the Eulerian grid without the usage of any particle-weight function. Formal procedure to determine the numerical accuracy of the LBS is yet to be developed. Case-by-case validation of the LBS method nevertheless has been conducted. Tan and Chu [26, 27] validated their LBS of wet water on dry bed by the exact analytical solution. Chu and Altai [4–6] compared their LBS of the laminar-and-turbulent interfaces with the experimental observations. In this paper, the numerical accuracy is assessed by the energy consideration in Sect. 7.

References

1. Adduce C, Sciortino G, Proietti S (2012) Gravity currents produced by lock exchanges: experiments and simulations with a two-layer shallow-water model with entrainment. J Hydraul Eng ASCE 138(2):111–121
2. Britter RE, Simpson JE (1978) Experiments on the dynamics of gravity current head. J Fluid Mech 88(part 2):223–240
3. Cantero MI, Lee JR, Balachandar S, García MH (2007) On the front velocity of gravity currents. J Fluid Mech 586:1–39
4. Chu VH, Altai W (2001) Simulation of shallow transverse shear flow by generalized second moment method. J Hydraul Res 39(6):575–582
5. Chu VH, Altai W (2012) Advection and diffusion simulations using Lagrangian blocks. Comput Therm Sci 4(4):351–363
6. Chu VH, Altai W (2015) Lagrangian block simulation of buoyancy at turbulence interfaces. Comput Therm Sci 7(2):181–189
7. Cantero MI, Balachandar S, Garcıa MH, Bock D (2008) Turbulent structures in planar gravity currents and their influence on the flow dynamics. J Geophys Res 113(C08018):1–22
8. Heezen BC, Ewing M (1952) Turbidity currents and submarine slumps, and the 1929 Grand Banks earthquake. Am J Sci 250:849–873
9. Hartel C, Meiburg E, Necker F (2000) Analysis and direct numerical simulation of the flow at a gravity-current head. Part 1. Flow topology and front speed for slip and no-slip boundaries. J Fluid Mech 418:189–212
10. Hartel C, Carlsson F, Thunblom M (2000) Analysis and direct numerical simulation of the flow at a gravity-current head. Part 2. The lobe-and-cleft instability. J Fluid Mech 418:213–229
11. Hsu SK, Kuo J, Lo CL, Tsai CH, Doo WB, Ku CY, Sibuet JC (2008) Turbidity currents, submarine landslides and the 2006 Pingtung earthquake off SW Taiwan. Terr Atmos Ocean Sci 19(6):762–772
12. Karimpour Ghannadi S, Chu VH (2015) High-order interpolation schemes for shear instability simulations. Int J Numer Methods Heat Fluid Flow 25(6):1340–1360
13. Lombardi V, Adduce C, Sciortino G, La Rocca M (2015) Gravity currents flowing upslope: laboratory experiments and shallow-water simulations. Phys Fluids 27:016602
14. Leonard BP (1995) Order of accuracy of QUICK. Appl Math Model 19:640–653
15. Marino BM, Thomas LP, Linden PF (2005) The front condition for gravity currents. J Fluid Mech 536:49–78
16. Monaghan JJ (2005) Smoothed particle hydrodynamics. Rep Prog Phys 68:1703–1759
17. Nogueira HIS, Adduce C, Alves E, Franca MJ (2013) Analysis of lock-exchange gravity currents over smooth and rough beds. J Hydraul Res 51(4):417–431
18. Nogueira H, Adduce C, Alves E, Franca M (2014) Dynamics of the head of gravity currents. Environ Fluid Mech 14:519–540
19. Ooi SK, Constantinescu G, Weber LJ (2007) 2D large-eddy simulation of lock-exchange gravity current flows at high Grashof numbers. J Hydraul Eng 133(9):1037–1047
20. Ooi SK, Constantinescu G, Weber L (2009) Numerical simulations of lock-exchange compositional gravity current. J Fluid Mech 635:361–388
21. Piper DJ, Cochonat P, Morrison ML (1999) The sequence of events around the epicentre of the 1929 Grand Banks earthquake: initiation of debris flows and turbidity current inferred from sidescan sonar. Sedimentology 46(1):79–97
22. Rottman JW, Simpson JE (1983) Gravity currents produced by instantaneous releases of a heavy fluid in a rectangular channel. J Fluid Mech 135:95–110
23. Shin JO, Dalziel SB, Linden PF (2004) Gravity currents produced by lock exchange. J Fluid Mech 521:1–34
24. Simpson JE (1982) Gravity currents in the laboratory, atmosphere and ocean. Annu Rev Fluid Mech 14:213–234
25. Thomas L, Dalziel S, Marino B (2003) The structure of the head of an inertial gravity current determined by particle-tracking velocimetry. Exp Fluids 34:708–716
26. Tan LW, Chu VH (2010) Wave runup simulations using Lagrangian blocks on Eulerian mesh. J Hydro-Environ Res 3(part 4):193–200
27. Tan L-W, Chu VH (2012) Two-dimensional simulation of shallow-water waves by Lagrangian block advection. Comput Fluids 65:35–43